

---

## **A Highly-Active and Stable Hydrogen Evolution Catalyst Based on Pyrite-Structured Cobalt Phosphosulfide**

Wen Liu,<sup>1</sup> Enyuan Hu,<sup>2</sup> Hong Jiang,<sup>3</sup> Yingjie Xiang,<sup>4</sup> Zhe Weng,<sup>1</sup> Min Li,<sup>5</sup> Qi Fan,<sup>1</sup> Xiqian Yu,<sup>2</sup> Eric I. Altman,<sup>5</sup> Hailiang Wang<sup>1\*</sup>

<sup>1</sup>Department of Chemistry and Energy Sciences Institute, Yale University, CT 06511, United States

<sup>2</sup>Brookhaven National Laboratory, Upton, New York 11973, United States

<sup>3</sup>Beijing National Laboratory for Molecular Sciences, College of Chemistry and Molecular Engineering, Peking University, 100871 Beijing, China

<sup>4</sup>Department of Mechanical Engineering and Materials Science, Yale University, CT 06511, United States

<sup>5</sup>Department of Chemical and Environmental Engineering, Yale University, CT 06511, United States

Correspondence to: [hailiang.wang@yale.edu](mailto:hailiang.wang@yale.edu)

**Rational design and controlled synthesis of hybrid structures comprising multiple components with distinctive functionalities are an intriguing and challenging approach to materials development for important energy applications like electrocatalytic hydrogen production where there is a great need for cost-effective, active and durable catalyst materials to replace the precious platinum. Here we report a structure design and sequential synthesis of a highly-active and stable hydrogen evolution electrocatalyst material based on pyrite-structured cobalt phosphosulfide nanoparticles grown on carbon nanotubes. The three synthetic steps in turn render electrical conductivity, catalytic activity, and stability to the material. The hybrid material exhibits superior activity for hydrogen evolution, achieving current densities of 10 and 100 mA cm<sup>-2</sup> at overpotentials of 48 and 109 mV respectively. Phosphorus substitution is crucial for the chemical stability and catalytic durability of the material, the molecular origins of which are uncovered by X-ray absorption spectroscopy and computational simulation.**

With the rising concern on energy crisis and environmental pollution, there has been a growing need to replace fossil fuels with clean and sustainable energy carriers. Molecular hydrogen with its high energy density and non-polluting characteristics, has been regarded as one of the most promising new fuels<sup>1,2</sup>. There are various methods to produce hydrogen, among which water splitting driven by electricity generated from renewable energy sources is an attractive way to support the future hydrogen economy. Efficient electrolytic hydrogen generation relies heavily on active, durable and affordable catalysts to accelerate the kinetics<sup>3,4,5</sup>. Although Pt has been widely acknowledged as the most active catalyst for the hydrogen evolution reaction (HER), this precious metal is scarce in the earth's crust and expensive for large scale applications.

In pursuit of inexpensive replacements for Pt as the HER electrocatalyst in acidic solutions, numerous inorganic materials based on non-precious transition metals, including sulfides<sup>6,7,8</sup>, selenides<sup>9,10</sup>, phosphides<sup>11,12,13</sup>, and others<sup>14,15</sup> have been explored. Extensive effort has been devoted to improving the HER catalytic activity of MoS<sub>2</sub> by identifying and exposing active sites<sup>6,16</sup> as well as enhancing electron conduction through nanostructuring<sup>17</sup>, shape control<sup>6,18</sup>, phase engineering<sup>19,20</sup>, doping<sup>21,22</sup>, intercalation<sup>23</sup> and hybridization<sup>17,24,25</sup>. Recently a ternary CoPS pyrite-type structure has been reported with superior catalytic activity for HER<sup>26</sup>. CoS<sub>2</sub> is another material of interest<sup>27,28</sup>. However, the existing HER catalyst materials based on non-noble metal elements are still less satisfactory in terms of both activity and stability, which calls for further material structure innovation to realize efficient and cost effective HER catalysis.

Here, we report a design and synthesis of a highly-active and stable HER electrocatalyst material consisting of pyrite-structured cobalt phosphosulfide (CoS|P) nanoparticles anchored on carbon nanotubes (CNTs). The material architecture is built by a three-step chemical synthesis: Strong interactions with CNTs and particle size control are first established by the selective growth of Co<sub>3</sub>O<sub>4</sub> nanoparticles on CNTs; High catalytic activity for HER is then rendered by conversion of Co<sub>3</sub>O<sub>4</sub> to CoS<sub>2</sub> nanoparticles; Good chemical stability and catalytic durability are lastly obtained from substituting part of the S with P. The unique material structure directly enables some of the highest HER catalytic performance among all Co-based catalyst materials. In 0.5 M H<sub>2</sub>SO<sub>4</sub>, the CoS|P/CNT hybrid exhibits a negligible onset overpotential and a Tafel slope of 55 mV dec<sup>-1</sup> with an exchange current density of 1.14 mA cm<sup>-2</sup>. At a mass loading of 1.6 mg cm<sup>-2</sup>, the hybrid material requires overpotentials of only 48 and 109 mV to reach stable catalytic current densities of 10 and 100 mA cm<sup>-2</sup> respectively, representing one of the few most active non-Pt catalysts for HER. P substitution in the pyrite structure is a critical step that renders chemical stability and catalytic durability to the CoS|P/CNT hybrid material. Density functional theory (DFT) calculations confirm the structural stability of pyrite CoS|P and suggest stronger metal-ligand bonding as a

contributor to the improved stability, which is supported by X-ray absorption spectroscopy data.

## Results

### Sequential synthesis of CoS|P/CNT

The synthetic strategy for the CoS|P/CNT hybrid material structure involves three steps, as illustrated in **Fig. 1**. In the first step,  $\text{Co}_3\text{O}_4$  nanoparticles were directly and selectively grown onto mildly oxidized multi-wall CNTs (see Supplementary Methods for CNT oxidation) by a hydrolysis reaction of cobalt acetate at 80 °C. An ethanol/water mixed solvent was used to slow down the hydrolysis reaction, facilitate interactions between the  $\text{Co}^{2+}$  and the functional groups on the CNT surface, and ensure selective nucleation and growth of  $\text{Co}_3\text{O}_4$  nanoparticles on CNTs.  $\text{NH}_3\cdot\text{H}_2\text{O}$  was added into the reaction system to coordinate the  $\text{Co}^{2+}$  and thus further reduce the hydrolysis rate to limit the size of the resulting  $\text{Co}_3\text{O}_4$  nanoparticles and optimize their distribution on the CNTs. Scanning electron microscopy (SEM), transmission electron microscopy (TEM) and X-ray diffraction (XRD) characterizations revealed the product structure as spinel structured  $\text{Co}_3\text{O}_4$  (PDF#43-1003) nanoparticles with an average size of 5-10 nm anchored on CNTs (**Supplementary Fig. 1**).

The second step is a hydrothermal reaction at 200 °C to convert  $\text{Co}_3\text{O}_4$  into  $\text{CoS}_2$ . Thioacetamide ( $\text{CH}_3\text{CSNH}_2$ ) was used as a slow-release S precursor which reacted with water to gradually generate the  $\text{H}_2\text{S}$  reactant and therefore allowed for facile chemical conversion from oxide to sulfide without damaging the material morphology and hybrid structure. SEM and TEM imaging showed nanoparticles with an average size of 10-20 nm attached to CNTs (**Supplementary Fig. 2a, b**). The nanoparticles were confirmed to be pyrite-structured  $\text{CoS}_2$  (PDF#41-1471) by XRD (**Supplementary Fig. 2d**). Lattice fringes of the  $\text{CoS}_2$  nanoparticles on CNTs were recorded with high-resolution TEM (**Supplementary Fig. 2c**). Energy dispersive spectroscopy (EDS) under scanning transmission electron microscopy (STEM) mode was used to map the distributions of elements of interest in the material structure. It is clear from the result that the nanoparticles consist of Co and S, and they are well anchored on the CNT surface (**Supplementary Fig. 3**).

The third step features a solid/gas-phase reaction at 400 °C to introduce P into the  $\text{CoS}_2$  structure.  $\text{NaH}_2\text{PO}_2\cdot\text{H}_2\text{O}$  was used as a precursor to generate the  $\text{PH}_3$  reactant via thermal decomposition. The  $\text{PH}_3$  then reacted with the  $\text{CoS}_2$  nanoparticles on CNTs to form the final CoS|P/CNT hybrid material. SEM and TEM characterizations confirmed the microstructure of nanoparticles with an average size of 10-20 nm on CNTs (**Fig. 2a, b**), suggesting that the substitution process had negligible influence on the material morphology and nanoparticle size. XRD measurement of the material generated a diffraction pattern characteristic of a pyrite structure with almost identical lattice parameters as  $\text{CoS}_2$  (**Fig. 2c**), indicating that the

substitution process happened in the form of P replacing S which did not alter the crystal structure or lattice parameters due to the very similar atomic sizes of S and P. The lattice fringes of the CoS|P nanoparticles were imaged by high-resolution TEM (**Fig. 2d**). The interplanar spacing of 0.277 nm corresponding to the (200) crystallographic planes of the pyrite structure is in consistency with the XRD result. The high-resolution TEM images also excluded the existence of core-shell structured nanoparticles.

### Structural and chemical analysis

To further understand the structure of the CoS|P/CNT hybrid material, STEM-EDS characterization was performed to gain elemental composition and distribution information. The EDS maps of Co, S and P overlap quite well (**Fig. 3a, b**), suggesting P has been uniformly doped into the crystal structure of nanoparticles. It is also evident from the EDS mapping that the CoS|P nanoparticles are closely anchored onto the CNT surfaces. The average atomic ratio of P/S in the nanoparticles was calculated to be  $\sim 1.0$  from the EDS spectrum (**Fig. 3c** and **Supplementary Fig. 4**), giving a  $\sim 50\%$  substitution of the S sites. Raman spectroscopy was used to probe chemical bonding information in the CoS|P nanoparticles. For the CoS<sub>2</sub>/CNT, two peaks were observed at 284 and 385 cm<sup>-1</sup> (**Fig. 3d**, blue trace). These Raman peaks could be attributed to the characteristic E<sub>g</sub> and A<sub>g</sub> vibrational modes corresponding to the in-phase stretching and pure libration of the S-S dumbbells in the pyrite structure<sup>29,30,31</sup>. For the CoS|P/CNT, the peaks slightly shifted to higher wavenumber (**Fig. 3d**, red trace) as a result of partial phosphorus substitution for sulfur and possible formation of P-S dumbbells. The characteristic Raman pattern also excludes formation of CoP<sup>32</sup>.

X-ray photoelectron spectroscopy (XPS) was employed to investigate the surface composition and oxidation states of the catalysts. For the CoS<sub>2</sub>/CNT, Co 2p<sub>3/2</sub> and 2p<sub>1/2</sub> core level peaks were observed at binding energies of 778.8 and 794.0 eV respectively together with satellite features (**Fig. 3e**), which matches literature results on CoS<sub>2</sub><sup>28</sup>. The Co 2p core level spectrum of the CoS|P/CNT hybrid is very similar to that of the CoS<sub>2</sub>/CNT, with binding energies of Co 2p<sub>3/2</sub> and 2p<sub>1/2</sub> peaks at 779.2 and 794.1 eV respectively (**Fig. 3e**). The negligible change in the Co 2p spectrum verifies that the oxidation state of Co is not affected by P substitution. The S 2p core level spectrum of the CoS<sub>2</sub>/CNT shows lower-binding-energy components at 162.6 and 163.9 eV (S 2p<sub>3/2</sub> and 2p<sub>1/2</sub>) attributed to sulfide species as well as higher-binding-energy components at 168.5 and 169.6 eV (S 2p<sub>3/2</sub> and 2p<sub>1/2</sub>) characteristic of sulfate species (**Fig. 3f**). Existence of the sulfate components suggests that the CoS<sub>2</sub>/CNT catalyst is slightly oxidized on surface. Interestingly, no sulfate features were found in the S 2p core level spectrum of the CoS|P/CNT (**Fig. 3f**), indicating P doping could prevent CoS<sub>2</sub> from oxidation under ambient conditions. The P 2p core level spectrum of the CoS|P/CNT

displays two peak regions (**Fig. 3g**), with one centered at the binding energy of 129.3 and 130.1 eV (P  $2p_{3/2}$  and  $2p_{1/2}$ ) which can be assigned to phosphorus anions and the other at 133.6 and 134.4 eV (unresolved doublet) characteristic of phosphate-like P. The existence of the high oxidation state P could be ascribed to surface oxidation under ambient conditions as often observed for metal phosphide materials<sup>33, 34, 35</sup>. Furthermore, a surface P/S ratio of  $\sim 1.0$  was derived from the XPS results, close to the bulk P/S ratio measured by EDS. This again corroborates that P is uniformly distributed within the nanoparticles rather than forming a shell-like structure on the original  $\text{CoS}_2$  nanoparticles.

### Electrocatalytic hydrogen evolution

HER electrocatalytic activity of the  $\text{CoS|P/CNT}$  hybrid material was assessed in 0.5 M  $\text{H}_2\text{SO}_4$  aqueous solution. **Fig. 4a** shows the polarization curve of the  $\text{CoS|P/CNT}$  hybrid material as compared to a benchmark Pt/C catalyst at a scan rate of  $5 \text{ mV s}^{-1}$ . With a mass loading of  $1.6 \text{ mg cm}^{-2}$ , the  $\text{CoS|P/CNT}$  electrode showed a negligible onset potential vs. the reversible hydrogen electrode (RHE). The catalytic current density increased rapidly with further cathodic polarization to 10, 20, and  $100 \text{ mA cm}^{-2}$  at overpotentials of 48, 65 and 109 mV respectively (**Fig. 4a**). An exchange current density of  $1.14 \text{ mA cm}^{-2}$  and a Tafel slope of 55 mV per decade were derived from the polarization curve (**Fig. 4b**), suggesting a different HER mechanism from Pt which showed a 30 mV per decade Tafel slope indicative of a Volmer-Tafel mechanism<sup>36</sup>. Such performance represents arguably higher HER catalytic activity than any other Co-based catalyst materials reported in the literature, placing our material at the top of all existing noble-metal-free HER catalyst materials working in acidic media (**Supplementary Table 1**). Our catalyst also showed high durability for HER catalysis. The initial current density ( $\sim 45 \text{ mA cm}^{-2}$ ) maintained after 24 hours of continuous hydrogen production (**Fig. 4c**). Stability for 100 hours of HER catalysis was also confirmed (**Supplementary Fig. 5**). We also performed 2000 cycles of cyclic voltammetry (CV) between 0.25 and  $-0.12 \text{ V}$  vs. RHE on the  $\text{CoS|P/CNT}$  catalyst. The polarization curves showed negligible shift during the test (**Fig. 4d**). Chronoamperometry in combination with gas chromatography and mass spectrometry (GC-MS) revealed Faradic efficiency of  $\sim 100\%$  for  $\text{H}_2$  (**Supplementary Fig. 6**).

### Discussion

The excellent HER catalytic activity and durability of the  $\text{CoS|P/CNT}$  hybrid material is a direct outcome of its unique material structure imparted by the three designed chemical reaction steps. The first step of reaction grows  $\text{Co}_3\text{O}_4$  nanoparticles on CNTs, which builds the strong electrical and chemical coupling between the nanoparticles and CNTs<sup>37, 38</sup>. Consequently, nanoparticles are anchored on the highly conductive CNT network which can

rapidly transport electrons from external circuit to nanoparticle/electrolyte interface for hydrogen evolution. This step also brings size control of the nanoparticles, which is essential for increasing the electrochemically active surface area and reducing the electron diffusion length within each nanoparticle.

The second step of reaction converts the  $\text{Co}_3\text{O}_4$  nanoparticles to  $\text{CoS}_2$  nanoparticles, through which highly active sites for HER catalysis are created. The  $\text{CoS}_2/\text{CNT}$  material is already as active as the final  $\text{CoS|P/CNT}$ . At a mass loading of  $0.8 \text{ mg cm}^{-2}$ , HER current density of  $10 \text{ mA cm}^{-2}$  was reached at an overpotential of 61 mV for the  $\text{CoS}_2/\text{CNT}$  as compared to 64 mV for the  $\text{CoS|P/CNT}$  under the same condition (**Supplementary Fig. 8a**). This already represents one of the most active cobalt chalcogenide HER catalyst materials<sup>10, 28, 39, 40, 41, 42</sup>. The sequential synthetic method, namely oxide growth followed by conversion to sulfide, is responsible for the superior catalytic activity, as corroborated by our control experiment (**Supplementary Fig. 7**).

In spite of the excellent activity as a result of size control and CNT hybridization, the intrinsic instability of  $\text{CoS}_2$  in strong acid is exacerbated. The  $\text{CoS}_2/\text{CNT}$  material is extremely unstable during HER catalysis in  $0.5 \text{ M H}_2\text{SO}_4$ . Under constant potential operation, the current density decreased drastically by 70% in less than 30 min (**Fig. 5a**). Such a dramatic deterioration was accompanied by substantial dissolution of the  $\text{CoS}_2$  active phase into the electrolyte. A Co concentration of  $\sim 2.1 \text{ ppm}$  in the electrolyte was measured by inductively coupled plasma mass spectrometry (ICP-MS) after 30 min of HER catalysis (**Fig. 5b**), corresponding to about 17.5% of the  $\text{CoS}_2$  having been dissolved. The concentration of dissolved Co gradually increased to  $\sim 2.9 \text{ ppm}$  over 20 h of HER operation. The  $\text{CoS}_2/\text{CNT}$  material is also sensitive to air and moisture. After being stored in ambient condition for 2 weeks, the  $\text{CoS}_2$  nanoparticles were completely oxidized to  $\text{CoSO}_4 \cdot 7\text{H}_2\text{O}$  (PDF#16-04872) which is soluble in water and HER inactive (**Fig. 5c**).

The third step of reaction (P substitution) is critical to the chemical stability and catalytic durability of the final material (**Fig. 5**, and **Supplementary Fig. 8**). No phase change was detected by XRD for the  $\text{CoS|P/CNTs}$  material after being stored in ambient condition for 2 weeks (**Fig. 5c**), suggesting significantly improved chemical stability to oxygen and moisture. This is consistent with our XPS results that P substitution could mitigate sulfate formation on  $\text{CoS}_2$  surface. The  $\text{CoS|P/CNTs}$  catalyst was able to sustain a current density of  $\sim 10 \text{ mA cm}^{-2}$  during 20 h of continuous HER operation (**Fig. 5a**), substantially more stable than the  $\text{CoS}_2/\text{CNT}$  catalyst under working conditions. In consistency, the amount of Co leaching into the electrolyte was much lower than that for the  $\text{CoS}_2/\text{CNT}$  catalyst. The Co concentration in electrolyte gradually reached  $\sim 0.6 \text{ ppm}$  within 12h and did not increase significantly in the following 8 h (**Fig. 5b**). To visually demonstrate the stability difference between the  $\text{CoS}_2/\text{CNT}$  and  $\text{CoS|P/CNT}$  in the electrolyte, we conducted a colorimetric comparison

(Supplementary Methods) after the CoS<sub>2</sub>/CNT and CoS|P/CNT hybrids were soaked in 0.5 M H<sub>2</sub>SO<sub>4</sub> for 2 h. The Nitrite R salt is widely used as a color indicator to detect cobalt in solution as it can form a red colored complex with Co<sup>2+</sup> ions. The solution in which the CoS<sub>2</sub>/CNT was soaked exhibited an orange color (**Fig. 5d**), clearly showing a considerable amount of Co dissolved into the acid. In contrast, the solution in which the CoS|P/CNT was soaked remained almost the same color as the blank control, confirming greatly improved stability of the CoS|P/CNT catalyst against acid corrosion. Our control experiment clearly verified that it is indeed the P substitution rather than the high-temperature annealing process that renders the excellent catalytic durability (**Supplementary Fig. 9**).

It is worth emphasizing here that the P substitution step is only for improving material stability and catalytic durability, but not for enhancing catalytic activity. This is different from the recent study where the CoPS is much more active than the CoS<sub>2</sub> with similar morphology<sup>26</sup>. It is also noted that our CoS|P is likely in a different structure than the recently reported CoPS. The CoPS is a distinct ternary pyrite-type phase featuring P-S bonds without any S-S bonds as in the CoS<sub>2</sub> pyrite structure. The corresponding XRD and Raman peaks significantly shifted as a result of the shrunk lattice parameters. In contrast, our CoS|P is more likely to be a CoS<sub>2</sub> pyrite structure (no lattice parameter shrinking) with some of the S atoms randomly substituted by P atoms. The structural difference is a direct outcome of the different synthetic methods adopted. The CoPS is prepared by converting Co(OH)(CO<sub>3</sub>)<sub>0.5</sub>·xH<sub>2</sub>O with pre-formed P<sub>x</sub>S<sub>y</sub>, therefore the P-S bonding is exclusive and CoPS is the only available composition. In this study, CoS|P is derived from CoS<sub>2</sub> so that the P/S ratio in the CoS<sub>2-x</sub>P<sub>x</sub>/CNT materials can be readily tuned between 0 and 1 while keeping the mother structure and lattice parameters unchanged (**Supplementary Fig. 10**). As we gradually increase the substitution level of P, the influence on HER activity is negligible but the catalytic durability improves drastically (**Supplementary Fig. 11**).

To probe the molecular origins of the structural stability of CoS|P/CNT, we performed X-ray absorption near edge structure (XANES) spectroscopy measurements. The absorption edges of the Co K-edge spectra of CoS<sub>2</sub>/CNT and CoS|P/CNT lie close to each other (**Fig. 6a**), suggesting similar oxidation states of Co in both materials, which match the XPS results. The relatively small pre-edge peaks of both spectra suggest that the Co ions invariably reside in octahedral coordination environment (**Fig. 6c**). It is noted that the CoS|P/CNT spectrum shows a shoulder peak at ~7717 eV. Similar features have been observed in other systems and are attributed to the covalency effect<sup>43</sup>. This correlates well with the pre-edge absorption intensity difference between the CoS|P/CNT and CoS<sub>2</sub>/CNT (inset of **Fig. 6a**). For both CoS|P and CoS<sub>2</sub>, the lowest unoccupied molecular orbitals are the anti-bonding e<sub>g</sub>\* orbitals<sup>44</sup>. These orbitals are due to hybridization between transition metal 3d and ligand 3p orbitals and are thus very sensitive to covalency. The stronger pre-edge adsorption of

CoS|P/CNT compared to that of CoS<sub>2</sub>/CNT suggests more p features in the Co 3d state and therefore stronger covalency for the CoS|P compound. Stronger covalency between the transition metal and ligands in CoS|P/CNT is also supported by the S K-edge XANES spectra. As shown in **Fig. 6b**, the CoS|P/CNT spectrum exhibits a stronger peak at ~2469 eV than the CoS<sub>2</sub>/CNT, corresponding to higher probability of 1s to e<sub>g</sub>\* transition as a result of stronger covalency of the metal-ligand bonds in CoS|P<sup>45</sup>.

To further rationalize the experimental findings, we performed first-principles DFT calculations for CoS<sub>2-x</sub>P<sub>x</sub> (x=0, 0.5, 1.0, 1.5 and 2) with both the cubic (pyrite) and monoclinic structures. The results for the relative stability of the two phases are shown in **Fig. 6d**. We found that CoS<sub>2</sub> is more stable in the cubic structure than in the monoclinic structure, but only with a marginal energy difference of about 0.03 eV per formula unit (f.u.). In contrast, CoP<sub>2</sub> is substantially more stable in the monoclinic structure by about 0.6 eV/f.u.. When S is substituted by P, the phosphosulfides would be more stable in the monoclinic structure within a large range of x if we assume a linear dependence of the relative stability of the two phases on the composition. However, first-principles calculations clearly suggest that CoS<sub>2-x</sub>P<sub>x</sub> is more stable in the cubic structure for x ≤ 1.0, which agrees well with our experimental results. The remarkable stability of the cubic structure can be attributed to the fact that cubic-phase CoS<sub>2</sub> and CoP<sub>2</sub> have very similar optimized equilibrium volume (V<sub>0</sub>) (41.6 vs. 40.1 Å<sup>3</sup>/f.u.). In comparison, the V<sub>0</sub> difference between monoclinic-phase CoS<sub>2</sub> and CoP<sub>2</sub> is much larger (42.8 vs. 39.2 Å<sup>3</sup>/f.u.). Substitution of S by P would induce much less strain in the cubic than in the monoclinic structure. Therefore, the pyrite-structured CoS<sub>2-x</sub>P<sub>x</sub> is stable within a quite wide range of P doping levels (x ≤ 1.0).

First-principles calculations can also provide insight into why incorporation of P improves the chemical stability of pyrite-structured CoS<sub>2</sub>. From projected density of states (PDOS) analysis (**Supplementary Fig. 12**), we see that P substitution significantly influences the nature of chemical bonding between Co and S/P. In the pyrite structure, each Co atom is coordinated in an octahedral ligand field (**Fig. 6c**), and therefore the 3d orbitals are split into t<sub>2g</sub> and e<sub>g</sub>\* manifolds that are of non-bonding and anti-bonding characteristics respectively. As qualitatively demonstrated in **Fig. 6e**, the highest occupied states in CoS<sub>2</sub> are of anti-bonding nature, which is the origin of the instability. When half of the S atoms are replaced by P which has fewer valence electrons, the anti-bonding e<sub>g</sub>\* orbitals are depleted, which strengthens the chemical bonding between Co and ligands and thus enhances the chemical stability of the material. This is in good agreement with our XANES results.

In conclusion, we demonstrate a novel structure design and synthesis of a highly-active and stable HER catalyst material based on pyrite-structured cobalt phosphosulfide. The sequential synthetic strategy we adopt imparts electrical conductivity, catalytic activity, and stability to the material. The CoS|P/CNT catalyst exhibits arguably the

highest catalytic activity among all non-noble metal based catalysts. P substitution is critical to chemical stability and catalytic durability of the material. The molecular origins are rationalized by spectroscopy characterization and computational modelling.

## Methods

### Material synthesis

The CoS|P/CNT hybrid was prepared through a 3-step method. In the first step (synthesis of Co<sub>3</sub>O<sub>4</sub>/CNT), 4 mg of mildly oxidized CNTs (the CNTs were oxidized following a modified Hummers method as described in Supplementary Information) were dispersed in 14 mL of ethanol by sonication for 1 h. Then, 0.8 mL of 0.2 M cobalt acetate aqueous solution and 0.6 mL of NH<sub>4</sub>OH (30%) were added to the suspension. The hydrolysis reaction was kept at 80 °C in oil bath with stirring for 12 h. After that, the product was collected by centrifuge. The precipitate was then washed with ethanol and DI water. The resulting Co<sub>3</sub>O<sub>4</sub>/CNT was lyophilized. To prepare CoS<sub>2</sub>/CNT, 20 mg of Co<sub>3</sub>O<sub>4</sub>/CNT was dispersed in 20 mL of DI water by sonication for 40 min, followed by the addition of 0.75 mL of 1M thioacetamide solution. After that, the reaction mixture was transferred to a 40 mL autoclave for hydrothermal reaction at 200 °C for 6 h. The resulting product was collected by centrifugation and repeated wash with DI water. The CoS<sub>2</sub>/CNT hybrid was then freeze-dried. In the third step, 5 mg of CoS<sub>2</sub>/CNT and 100 mg of NaH<sub>2</sub>PO<sub>2</sub>·H<sub>2</sub>O were placed at two separate positions in a ceramic crucible with the NaH<sub>2</sub>PO<sub>2</sub>·H<sub>2</sub>O at the upstream side. The samples were heated at 400 °C for 1 h with Ar gas flowing at 200 sccm. The final product contains about 60 wt% of CoS|P and 40 wt% of CNTs.

### Electrochemical measurements

To prepare catalyst ink, 1 mg of CoS|P/CNT was mixed with 190 µL of water, 50 µL of ethanol, and 10 µL of 5 wt% Nafion solution by sonication for 1 h. Subsequently, 50-200 µL of the catalyst ink was drop-dried onto a carbon fiber paper (Spectracarb 2050A from Fuel Cell Store) to cover an area of 0.5 cm<sup>2</sup> (0.4-1.6 mg cm<sup>-2</sup>). The electrode was further heated at 90 °C in vacuum for 2 h. HER catalytic measurements were performed with a CHI 760D electrochemistry workstation (CH instruments, USA). A conventional three electrode cell configuration was employed. A saturated calomel electrode (SCE) was used as the reference electrode, and a graphite rod was used as the counter electrode. 0.5 M H<sub>2</sub>SO<sub>4</sub> solution was used as electrolyte. Linear sweep voltammetry was recorded at a scan rate of 5 mV s<sup>-1</sup>. All the polarization curves were iR-corrected. The reference electrode was calibrated against the reversible hydrogen electrode (RHE) as shown in **Supplementary Fig. 13**. All the potentials reported in our work were converted according to  $E(\text{vs. RHE}) = E(\text{vs. SCE}) + 0.278 \text{ V}$ .

### First-Principles calculations

All DFT calculations were conducted by using the Vienna ab-initio simulation package (VASP)

---

suite that is based on the projector-augmented wave (PAW) approach and the plane wave basis set<sup>46</sup>. The structures of  $\text{CoS}_{2-x}\text{P}_x$  ( $x=0, 0.5, 1.0, 1.5$  and  $2$ ), including lattice constants and internal coordinates, in both the cubic (pyrite) and monoclinic phases were optimized using the Perdew-Burke-Ernzerhof<sup>47</sup> approximation for the exchange-correlation functional with a plane wave energy cutoff of 400 eV, which is about 1.5 times of the default cutoff value such that the Pulay stress problem can be avoided. To account for the possible strong correlation effects in the Co 3d electrons, the energy difference between the cubic and monoclinic phases was calculated using the PBE plus the Hubbard  $U$  correction (PBE+ $U$ ) approach in the rotationally invariant scheme (LDAUTYPE=1)<sup>48</sup> with  $U=4.5$  eV and  $J=0.5$  eV. We used the special quasi-random structure approach<sup>49</sup> implemented in the ATAT code<sup>50</sup> to model the random substitution of S by P in  $\text{CoS}_{2-x}\text{P}_x$  using a supercell of 24 atoms.

### **Acknowledgements**

The work is partially supported by Yale University and the Global Innovation Initiative from Institute of International Education. The work at BNL was supported by the U.S. Department of Energy, the Assistant Secretary for Energy Efficiency and Renewable Energy, Office of Vehicle Technologies under Contract Number DE-SC0012704. The authors acknowledge technical support from the scientists at beamlines 9-BM-B and 12-BM-B of APS (ANL), supported by the U.S. DOE under Contract No. DE-AC02-06CH11357. M.L. and E.I.A. acknowledge the support of the U.S. Department of Energy through Basic Energy Sciences grant DE-FG02-98ER14882 and the use of facilities supported by the National Science Foundation through the Yale Materials Research Science and Engineering Center (Grant No. MRSEC DMR-1119826). The authors thank Prof. Fei Wei (Tsinghua University) for providing the CNTs. The authors appreciate acquisition of XPS spectra by Baowen Li (CMCM IBS Center, Ulsan National University of Science and Technology).

### **Author contributions**

W.L. and H.W. conceived the research. W.L. and Y.X. synthesized the materials and performed the electrochemical measurements. E.H. performed the XANES measurements. H.J. performed the DFT calculations. W.L., Z.W., M.L. and Q.F. performed the material characterizations. All authors discussed and analyzed the data. W.L., E.H., H.J. and H.W. wrote the paper. All authors discussed and commented on the manuscript.

### **Additional information**

The authors declare no competing financial interests. Supplementary information is available in the online version of the paper. Reprints and permissions information is available online at [www.nature.com/reprints](http://www.nature.com/reprints). Correspondence and requests for materials should be addressed

to H.W.

## References

1. Turner JA. Sustainable hydrogen production. *Science* **305**, 972-974 (2004).
2. Mazloomi K, Gomes C. Hydrogen as an energy carrier: Prospects and challenges. *Renew. Sustainable Energy Rev.* **16**, 3024-3033 (2012).
3. Yang J, Shin HS. Recent advances in layered transition metal dichalcogenides for hydrogen evolution reaction. *J. Mater. Chem. A* **2**, 5979-5985 (2014).
4. Faber MS, Jin S. Earth-abundant inorganic electrocatalysts and their nanostructures for energy conversion applications. *Energy Environ. Sci.* **7**, 3519-3542 (2014).
5. Zou X, Zhang Y. Noble metal-free hydrogen evolution catalysts for water splitting. *Chem. Soc. Rev.* **44**, 5148-5180 (2015).
6. Jaramillo TF, Jorgensen KP, Bonde J, Nielsen JH, Horch S, Chorkendorff I. Identification of active edge sites for electrochemical H<sub>2</sub> evolution from MoS<sub>2</sub> nanocatalysts. *Science* **317**, 100-102 (2007).
7. Laursen AB, Kegnaes S, Dahl S, Chorkendorff I. Molybdenum sulfides-efficient and viable materials for electro- and photoelectrocatalytic hydrogen evolution. *Energy Environ Sci* **5**, 5577-5591 (2012).
8. Voiry D, *et al.* Enhanced catalytic activity in strained chemically exfoliated WS<sub>2</sub> nanosheets for hydrogen evolution. *Nat. Mater.* **12**, 850-855 (2013).
9. Wang H, *et al.* MoSe<sub>2</sub> and WSe<sub>2</sub> nanofilms with vertically aligned molecular layers on curved and rough surfaces. *Nano Lett.* **13**, 3426-3433 (2013).
10. Kong D, Wang H, Lu Z, Cui Y. CoSe<sub>2</sub> nanoparticles grown on carbon fiber paper: an efficient and stable electrocatalyst for hydrogen evolution reaction. *J. Am. Chem. Soc.* **136**, 4897-4900 (2014).
11. McEnaney JM, *et al.* Amorphous Molybdenum Phosphide Nanoparticles for Electrocatalytic Hydrogen Evolution. *Chem. Mater.* **26**, 4826-4831 (2014).
12. Jiang P, Liu Q, Liang Y, Tian J, Asiri AM, Sun X. A cost-effective 3D hydrogen evolution cathode with high catalytic activity: FeP nanowire array as the active phase. *Angew. Chem. Int. Ed. Engl.* **53**, 12855-12859 (2014).
13. Liu Q, *et al.* Carbon Nanotubes Decorated with CoP Nanocrystals: A Highly Active Non-Noble-Metal Nanohybrid Electrocatalyst for Hydrogen Evolution. *Angew. Chem. Int. Ed.* **53**, 6710-6714 (2014).
14. Li YH, *et al.* Local atomic structure modulations activate metal oxide as electrocatalyst for hydrogen evolution in acidic water. *Nat Commun* **6**, 8064 (2015).
15. Yan HJ, *et al.* Phosphorus-Modified Tungsten Nitride/Reduced Graphene Oxide as a High-Performance, Non-Noble-Metal Electrocatalyst for the Hydrogen Evolution Reaction. *Angew. Chem. Int. Ed.* **54**, 6325-6329 (2015).
16. Kong D, *et al.* Synthesis of MoS<sub>2</sub> and MoSe<sub>2</sub> films with vertically aligned layers. *Nano Lett.* **13**, 1341-1347 (2013).
17. Li YG, Wang HL, Xie LM, Liang YY, Hong GS, Dai HJ. MoS<sub>2</sub> Nanoparticles Grown on Graphene: An Advanced Catalyst for the Hydrogen Evolution Reaction. *J. Am. Chem. Soc.* **133**, 7296-7299 (2011).
18. Yang Y, Fei H, Ruan G, Xiang C, Tour JM. Edge-oriented MoS<sub>2</sub> nanoporous films as flexible electrodes for hydrogen evolution reactions and supercapacitor devices. *Adv. Mater.* **26**, 8163-8168 (2014).
19. Voiry D, *et al.* Conducting MoS<sub>2</sub> nanosheets as catalysts for hydrogen evolution reaction. *Nano Lett.* **13**, 6222-6227 (2013).
20. Morales-Guio CG, Hu X. Amorphous molybdenum sulfides as hydrogen evolution catalysts. *Acc.*

- 
- Chem. Res.* **47**, 2671-2681 (2014).
21. Kibsgaard J, Jaramillo TF. Molybdenum Phosphosulfide: An Active, Acid-Stable, Earth-Abundant Catalyst for the Hydrogen Evolution Reaction. *Angew. Chem. Int. Ed.* **53**, 14433-14437 (2014).
  22. Deng J, *et al.* Triggering the electrocatalytic hydrogen evolution activity of the inert two-dimensional MoS<sub>2</sub> surface via single-atom metal doping. *Energy Environ Sci* **8**, 1594-1601 (2015).
  23. Wang H, *et al.* Electrochemical tuning of vertically aligned MoS<sub>2</sub> nanofilms and its application in improving hydrogen evolution reaction. *Proc. Natl. Acad. Sci. U. S. A.* **110**, 19701-19706 (2013).
  24. Wang T, *et al.* Electrochemically fabricated polypyrrole and MoS<sub>x</sub> copolymer films as a highly active hydrogen evolution electrocatalyst. *Adv. Mater.* **26**, 3761-3766 (2014).
  25. Gao MR, *et al.* An efficient molybdenum disulfide/cobalt diselenide hybrid catalyst for electrochemical hydrogen generation. *Nat Commun* **6**, 5982 (2015).
  26. Caban-Acevedo M, *et al.* Efficient hydrogen evolution catalysis using ternary pyrite-type cobalt phosphosulfide. *Nat. Mater.* **14**, 1245-1251 (2015).
  27. Zhang H, *et al.* Highly Crystallized Cubic Catterite CoS<sub>2</sub> for Electrochemically Hydrogen Evolution over Wide pH Range from 0 to 14. *Electrochim. Acta* **148**, 170-174 (2014).
  28. Faber MS, Dzedzic R, Lukowski MA, Kaiser NS, Ding Q, Jin S. High-performance electrocatalysis using metallic cobalt pyrite CoS<sub>2</sub> micro- and nanostructures. *J. Am. Chem. Soc.* **136**, 10053-10061 (2014).
  29. Anastassakis E. Light scattering and ir measurements in XS<sub>2</sub> pyrite-type compounds. *J Chem Phys* **64**, 3604 (1976).
  30. Lyapin S, Utyuzh A, Petrova A, Novikov A, Lograsso T, Stishov S. Raman studies of nearly half-metallic ferromagnetic CoS<sub>2</sub>. *J. Phys.: Condens. Matter* **26**, 396001 (2014).
  31. Shadike Z, Cao MH, Ding F, Sang L, Fu ZW. Improved electrochemical performance of CoS<sub>2</sub>-MWCNT nanocomposites for sodium-ion batteries. *Chem Commun (Camb)* **51**, 10486-10489 (2015).
  32. Ma LB, Shen XP, Zhou H, Zhu GX, Ji ZY, Chen KM. CoP nanoparticles deposited on reduced graphene oxide sheets as an active electrocatalyst for the hydrogen evolution reaction. *J. Mater. Chem. A* **3**, 5337-5343 (2015).
  33. Jiang J, *et al.* Synthesis of FeP<sub>2</sub>/C nanohybrids and their performance for hydrogen evolution reaction. *J. Mater. Chem. A* **3**, 499-503 (2015).
  34. Pu Z, Liu Q, Asiri AM, Sun X. Tungsten phosphide nanorod arrays directly grown on carbon cloth: a highly efficient and stable hydrogen evolution cathode at all pH values. *ACS Appl. Mater. Interfaces* **6**, 21874-21879 (2014).
  35. Xiao M, Miao Y, Tian Y, Yan Y. Synthesizing Nanoparticles of Co-P-Se compounds as Electrocatalysts for the Hydrogen Evolution Reaction. *Electrochim. Acta* **165**, 206-210 (2015).
  36. Saraby-Reintjes A. Kinetic criteria for the mechanism of the hydrogen evolution reaction. *Electrochimica Acta* **31**, 251-254 (1986).
  37. Fan Q, Liu W, Weng Z, Sun Y, Wang H. Ternary Hybrid Material for High-Performance Lithium-Sulfur Battery. *J. Am. Chem. Soc.* **137**, 12946-12953 (2015).
  38. Weng Z, *et al.* Metal/Oxide Interface Nanostructures Generated by Surface Segregation for Electrocatalysis. *Nano Lett.* **15**, 7704-7710 (2015).
  39. Kong D, Cha JJ, Wang H, Lee HR, Cui Y. First-row transition metal dichalcogenide catalysts for hydrogen evolution reaction. *Energy Environ Sci* **6**, 3553-3558 (2013).
  40. Peng S, *et al.* Cobalt sulfide nanosheet/graphene/carbon nanotube nanocomposites as flexible

- 
- electrodes for hydrogen evolution. *Angew. Chem. Int. Ed. Engl.* **53**, 12594-12599 (2014).
41. Zhang H, Li Y, Zhang G, Xu T, Wan P, Sun X. A metallic CoS<sub>2</sub> nanopyramid array grown on 3D carbon fiber paper as an excellent electrocatalyst for hydrogen evolution. *J. Mater. Chem. A* **3**, 6306-6310 (2015).
  42. Liu Q, Shi J, Hu J, Asiri AM, Luo Y, Sun X. CoSe<sub>2</sub> nanowires array as a 3D electrode for highly efficient electrochemical hydrogen evolution. *ACS Appl. Mater. Interfaces* **7**, 3877-3881 (2015).
  43. Gyu Kim M, Sang Cho H, Hyun Yo C. Fe K-edge X-Ray Absorption (XANES/EXAFS) Spectroscopic Study of the Nonstoichiometric SrFe<sub>1-x</sub>Sn<sub>x</sub>O<sub>3-y</sub> System. *J. Phys. Chem. Solids* **59**, 1369-1381 (1998).
  44. Bither TA, Bouchard RJ, Cloud WH, Donohue PC, Siemons WJ. Transition Metal Pyrite Dichalcogenides High-Pressure Synthesis and Correlation of Properties. *Inorg. Chem.* **7**, 2208-2220 (1968).
  45. Sugiura C. Sulfur-K X-Ray Absorption-Spectra of FeS, FeS<sub>2</sub>, and Fe<sub>2</sub>S<sub>3</sub>. *J. Chem. Phys.* **74**, 215-217 (1981).
  46. Kresse G, Furthmuller J. Efficiency of ab-initio total energy calculations for metals and semiconductors using a plane-wave basis set. *Computational Materials Science* **6**, 15-50 (1996).
  47. Perdew JP, Burke K, Ernzerhof M. Generalized Gradient Approximation Made Simple. *Phys. Rev. Lett.* **77**, 3865-3868 (1996).
  48. Liechtenstein AI, Anisimov VV, Zaanen J. Density-functional theory and strong interactions: Orbital ordering in Mott-Hubbard insulators. *Phys Rev B Condens Matter* **52**, R5467-R5470 (1995).
  49. Wei S, Ferreira LG, Bernard JE, Zunger A. Electronic properties of random alloys: Special quasirandom structures. *Phys Rev B Condens Matter* **42**, 9622-9649 (1990).
  50. van de Walle A. Multicomponent multisublattice alloys, nonconfigurational entropy and other additions to the Alloy Theoretic Automated Toolkit. *Calphad-Computer Coupling of Phase Diagrams and Thermochemistry* **33**, 266-278 (2009).

---

## Figure Captions

**Figure 1: Schematic illustration of the sequential synthesis of the CoS|P/CNT hybrid material for HER catalysis.** The CoS|P/CNT is synthesized through three steps including hydrolysis, hydrothermal sulfurization, and solid/gas-phase phosphorization.

**Figure 2: Structural characterizations of the CoS|P/CNT hybrid material. (a)** SEM image of CoS|P/CNT; Scale bar, 200 nm. **(b)** Low-magnification TEM image of CoS|P/CNT showing nanoparticles attached to CNTs; Scale bar, 20 nm. **(c)** XRD pattern of CoS|P/CNT as compared with the pyrite-phase CoS<sub>2</sub> standard (PDF#41-1471). **(d)** High-resolution TEM image showing the (200) lattice fringes of pyrite-phase CoS|P; Scale bar, 5 nm.

**Figure 3. Composition and chemical analysis for the CoS|P/CNT hybrid material. (a)** STEM image recorded by a high angle annular dark field (HAADF) detector showing CoS|P nanoparticles attached on CNTs. Scale bar is 20 nm. **(b)** STEM-EDS mapping of CoS|P/CNT catalyst showing the distributions of Co (green), P (yellow) and S (orange) within the nanoparticles closely attached to C (red). Scale bar, 20 nm. **(c)** EDS spectrum of CoS|P/CNT. **(d)** Raman spectra of CoS<sub>2</sub>/CNT and CoS|P/CNT. **(e-g)** Co 2p, S 2p and P 2p core level XPS spectra of CoS|P/CNT and CoS<sub>2</sub>/CNT.

**Figure 4: Electrocatalytic hydrogen evolutions over the CoS|P/CNT catalyst. (a)** Polarization curves for HER on the CoS|P/CNT hybrid and a commercial Pt/C catalyst at 5 mV s<sup>-1</sup>. The catalyst mass loading was 0.4 mg cm<sup>-2</sup> for Pt/C catalyst. **(b)** Tafel plots for the CoS|P/CNT and Pt/C catalysts derived from the polarization curves in **a**. **(c)** Chronoamperometric response ( $j \sim t$  curve) recorded on the CoS|P/CNT electrode at a constant overpotential of 95mV with iR compensation. **(d)** CV test between 0.25 and -0.12 V vs. RHE at a scan rate of 100 mV s<sup>-1</sup> for 2000 cycles. The catalyst mass loading of CoS|P/CNT was 1.6 mg cm<sup>-2</sup> unless otherwise noted.

**Figure 5: Comparison of chemical stability and catalytic durability between CoS<sub>2</sub>/CNT and CoS|P/CNT. (a)** Typical chronoamperometric responses ( $j \sim t$  curves) of the CoS<sub>2</sub>/CNT and CoS|P/CNT catalysts driving hydrogen evolution at the overpotential of 77 mV without iR compensation for 20 h in 0.5 M H<sub>2</sub>SO<sub>4</sub> solution. 0.4 mg of each catalyst was loaded on a carbon fiber paper with 0.5 cm<sup>2</sup> of active area. The sharp current fluctuations were caused by the sampling of electrolyte during the electrolysis process. **(b)** Boxplots (median and quartiles) representing the concentrations of Co dissolved in 20 ml of electrolyte as the HER catalysis proceeds. The vertical whiskers represent the standard deviations. The statistics are

derived from at least 3 independent measurements. **(c)** XRD patterns of CoS<sub>2</sub>/CNT and CoS|P/CNT after 2 weeks of storage in ambient conditions. **(d)** Colorimetric comparison of the CoS<sub>2</sub>/CNT and CoS|P/CNT hybrids soaked in 0.5 M H<sub>2</sub>SO<sub>4</sub> solution for 2 h; Nitrite R salt was used as the color indicator.

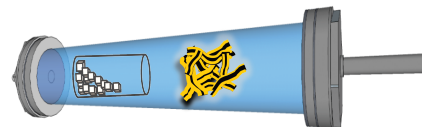
**Figure 6: XANES spectra of CoS|P/CNT and structural stability discussion based on First Principles Calculations.** **(a)** Cobalt K-edge XANES spectra of CoS<sub>2</sub>/CNT and CoS|P/CNT compared with Co<sup>II</sup> (CoO) and Co<sup>III</sup> (LiCoO<sub>2</sub>) standards. Pre-edge features correspond to transition from 1s (Co) orbital to e<sub>g</sub>\* anti-bonding state which is metal 3d and ligand 3p hybrid orbitals. The pre-edge features were fitted by two pseudo-Voigt functions with the results shown in the inset graph. **(b)** Sulfur K-edge XANES spectra of CoS<sub>2</sub>/CNT and CoS|P/CNT. **(c)** Structure illustration of pyrite-phase CoS<sub>2</sub> and CoS|P (CoS<sub>2-x</sub>P<sub>x</sub>, x=1), each with a representative coordination polyhedron. **(d)** The energy difference per formula unit (f.u.) between the cubic and monoclinic phases as a function of the P substitution extent obtained from DFT calculations. The inset shows the equilibrium volume per f.u. in the cubic and monoclinic phases as a function of the P substitution extent. **(e)** Conceptual energy level diagrams of the frontier molecular orbitals for pyrite-phase CoS<sub>2</sub> and CoS|P derived from the calculated electronic structures (**Supplementary Fig. 12**). CoS<sub>2</sub> is magnetic at room temperature. As a result spin-up and spin-down electrons have different energy levels. CoS|P (CoS<sub>2-x</sub>P<sub>x</sub>, x=1) is non-magnetic.



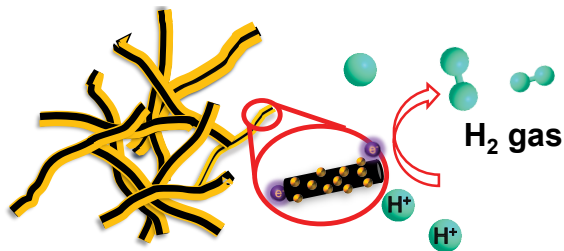
$\text{CNT} + \text{Co}(\text{OAc})_2 + \text{NH}_3 \cdot \text{H}_2\text{O}$   
80 °C, 12 h



$\text{Co}_3\text{O}_4/\text{CNT} + \text{CH}_3\text{CSNH}_2$   
200 °C, 6 h



$\text{CoS}_2/\text{CNT} + \text{NaH}_2\text{PO}_2 \cdot \text{H}_2\text{O}$   
400 °C, 1 h



**CoS|P/CNT hybrid for HER**

